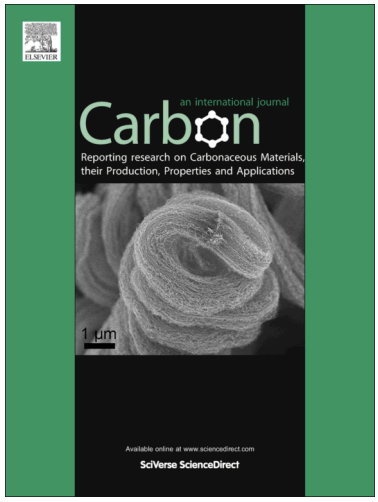

Raman Study of Damage Extent in Graphene Nanostructures Carved by High Energy Helium Ion Beam

Shuojin Hang, Zakaria Moktadir, Hiroshi Mizuta

PII: S0008-6223(14)00129-8
DOI: http://dx.doi.org/10.1016/j.carbon.2014.01.071
Reference: CARBON 8745

To appear in: *Carbon*

Received Date: 12 November 2013
Accepted Date: 31 January 2014

Please cite this article as: Hang, S., Moktadir, Z., Mizuta, H., Raman Study of Damage Extent in Graphene Nanostructures Carved by High Energy Helium Ion Beam, *Carbon* (2014), doi: http://dx.doi.org/10.1016/j.carbon.2014.01.071

Raman Study of Damage Extent in Graphene Nanostructures Carved by High Energy Helium Ion Beam

Shuojin Hang[1*], *Zakaria Moktadir*[1], *Hiroshi Mizuta*[1,2]

[1]Faculty of Physical Sciences and Engineering, University of Southampton, University of Southampton, Highfield, Southampton, SO17 1BJ, United Kingdom

[2]Japan Advanced Institute of Science and Technology, 1-1 Asahi-dai, Nomi, Ishikawa, 923-1292, Japan

ABSTRACT: We performed spatial Raman mapping on supported monolayer graphene carved by 30keV He^+ beam. A tilt beam was introduced to effectively eliminate the substrate swelling. The ratio between D and G peak intensities shows that Stage 1 and Stage 2 disorder are introduced over a wider range on both sides of the 35 nm etched line. The mean defect distance L_D was estimated in these regions using the local activation model. Vacancies and amorphisations are dominant type of defects as suggested by the ratio of D and D' peak intensities. Monte Carlo simulation on stopping range of ions was accomplished to explain the asymmetric defect formation in graphene.

[*] Corresponding author: Tel: +44(0)23 8059 3126, E-mail: sh13g08@ecs.soton.ac.uk (Shuojin Hang)

1. Introduction

Graphene has attracted enormous interests thanks to its extraordinary electronic[1–3], optical[4] and mechanical properties[5] since its discovery in 2004[6]. The intrinsic properties of graphene strongly depend on its geometry owing to its unique 2D nature. One notable example is the band-gap engineering on graphene nanoribbons (GNR)[7]. Furthermore, lithographically defined quantum dots are effective structures for building a spin qubit, the building block for quantum information technology[8–11]. In spite of the recent rapid development in the field, these applications face the problem of downscaling beyond conventional e-beam lithography. Various approaches have been explored, which can be categorized as 1) bottom-up and 2) top-down. In the former case, 1-D device such as extremely thin GNR with well-defined edges and widths are synthesized chemically, but a follow-up step is usually needed to selectively transfer the good GNR to the desired substrate[12,13]. On the other hand, the top-down methods aggressively reduces the feature size by direct writing involving electron/ion bombardment[14–18]. One can increase the particle's momentum (reducing wavelength) either by accelerating the particle or using a heavier ion to reduce the particle wavelength thus achieving high resolution. Sub-1nm resolution has previously been demonstrated by accelerating electrons at 200kV in a transmission electron microscope (TEM)[15]. An alternative approach is using a tightly focused He^+ beam accelerated at 30kV[14,16]. In both cases, GNR of ~5nm were fabricated. In fact, almost any pattern with achievable size can be carved using this direct-writing technology showing the main advantage of the top-down methods[17].

However, despite the high resolution and the ease of pattern choice, most of the above-mentioned top-down approaches were carried out on suspended graphene, limiting its usefulness for many practical applications where a substrate is needed[19,20]. In addition, suspended graphene devices are difficult to handle and are not suitable for many practical applications. On

the other hand, recent progress on the quasi-suspended graphene made by stacking with other 2-D materials has shown superior properties implying that a structural suspension may no longer be necessary for many high performance devices[20–22]. The mechanisms at play during the carving of suspended graphene and supported graphene can be very different owing to the complex interaction between ion/electron beams and the substrate material[23]. For instance, atomic simulation suggests that supported graphene has much larger displacement threshold compared to suspended graphene[24]. Lastly, due to the tininess of the device structures, there is yet an effective way to examine the damage on graphene after fabrication. High resolution TEM (HRTEM) is a powerful method to investigate the formation and evolution of defects[25,26], edges[27] and grain boundaries[28] in graphene owing to its atomic resolution. However this approach has several limitations. Firstly, the sample needs to be suspended before imaging while our emphasis in this work is on the examination of damage extent in a graphene-on-substrate system, rather than examining suspended graphene nanostructures. Secondly, the sample needs to be perfectly clean to avoid beam-induced etching where extended holes nucleate at contamination sites[26,29,30]. In this context, we deem HRTEM not suitable for our particular study since further exposure to high energy electrons may cause evolution of defects in our already-defected samples, thus making the result inaccurate.

Raman spectroscopy is a well-established non-destructive method that monitors the structural and electronic properties of graphitic materials [31–36]. Although the Raman mapping process lacks the atomic resolution of HRTEM, the spectrum at each data point precisely reflects the defect density in the sample through the scattering of photons which is closely related to the lattice structure of the sample under test. Here we propose a new way of determining the extent of the damage in ion beam carved graphene using Raman spectroscopy. We show that backscattered ions and other dislodged substrate atoms are a major source of damage and we

propose solutions to minimize the amount of defects in the useful areas of patterned graphene nanodevices.

The Raman spectrum of pristine graphene consists of two distinctive features, known as G and 2D peaks which are located at around 1580 cm^{-1} and 2680 cm^{-1}, respectively. The G peak originates from the high frequency E_{2g} optical phonon while the 2D peak is associated with the breathing mode of graphene hexagonal ring[32]. The presence of defects gives rise to another two features at around 1345 cm^{-1} (D peak) and 1600 cm^{-1} (D' peak), which initially are forbidden in non-defective graphene as a result of Raman selection rule. Being the undertone of 2D, D is also associated with the breathing mode of the honeycomb structure and is activated by the intervalley scattering of single phonon [32]. We will focus on G, D, and D' peaks because they contain information about defect density[34,35,37,38] and defect type[38,39].

The evolution of disorder in graphene can be categorized in two stages (denoted 'Stage 1' and 'Stage 2') as described by a local activation model[34]. The dependence of I(D)/I(G) on the the mean distance L_D between two defects is given by:

$$I(D)/I(G) = C_A \frac{r_A^2 - r_S^2}{r_A^2 - 2r_S^2}\left[e^{(-\pi r_S^2/L_D^2)} - e^{(-\pi(r_A^2 - r_S^2/L_D^2)}\right] + C_S\left(1 - e^{(-\pi r_S^2/L_D^2)}\right) \quad (1)$$

A Raman active region is defined by two length scales r_S and r_A, which are the radii of the structurally disordered region (S-region) and the surrounding activated region (A-region), respectively[34]. The phonon scattering contributes to D peak only if the e-h excitation is created in the A-region, otherwise it will either enhance G peak for e-h created outside S- and A- regions or suppress the D peak if it falls into S-region only. In Stage 1 when defect density is relatively low, the area of A-region expands with defect density causing I(D)/I(G) to increase. When defect density is sufficiently large that the whole area is covered by S- and A-regions, the fraction of A-region saturates marking the onset of Stage 2. In Stage 2, A-region converts to S-region as more

defects are created giving rise to the decrease of I(D)/I(G) due to the loss of hexagonal rings. Therefore the non-monotonic change of I(D)/I(G) is a consequence of the balance of S- and A-regions, weighted by parameter C_A and C_S. The critical value of L_D at the transition of two stages is estimated by $L_D \approx \ _F / \ _D$=4nm, where $\ _F$ is the Fermi velocity and $\ _D$ is the Debye cut-off frequency[40].

We show that milling will create defects of various degrees near the milling site by analyzing the spatially resolved Raman map. By using the above-mentioned model, L_D can be quantified locally. We will be using the following notations: 1) I(D), I(G) and I(D') for intensity of D, G and D' peak, respectively 2) (G) for the full width at half maximum (FWHM) of G peak 3) I(D)/I(G) for the ratio of I(D) to I(G) 4) I(D)/I(D') for the ration of I(D) to I(D').

2. Experimental

Graphene flakes were prepared by mechanical exfoliation of highly oriented pyrolytic graphite on a 300 nm SiO_2 substrate. Single layer flakes were identified using both an optical contrast method and Raman spectroscopy[31]. As shown in Fig. 1, the Raman spectrum show a G peak at ~1587 cm^{-1} and a sharp 2D peak at ~2680 cm^{-1} with a ratio I(2D)/I(G)~2.37 . No D peak at ~ 1344 cm^{-1} was observed in pristine samples. No significant shifts of all the peaks were observed. A Zeiss ORION scanning helium ion microscope (HIM) was used for precision patterning [16–18,41–44]. We consistently accelerated He^+ ions at 30kV to obtain good image brightness and contrast. The beam current was maintained at 1pA. The patterning resolution was 1 pixel/nm^2 and the dwell time on each pixel was 3μs. Fig. 1 shows the evolution of Raman spectrum of the same single layer graphene flake which was subjected to an increasing He^+ irradiation dose. The dose for rough imaging is around three orders of magnitude smaller than

the dose used for milling and shows little damage on graphene as verified by Raman spectroscopy.

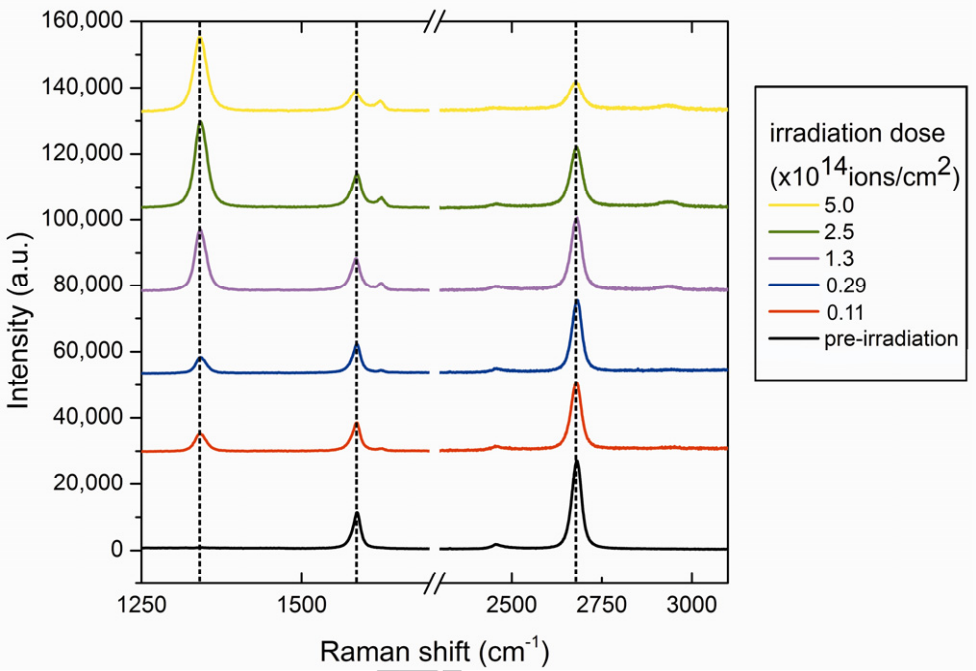

Fig. 1. Raman spectra of a single layer graphene before and after the irradiation of 30 kV He^+ ions at various doses.

We first conducted milling tests at various conditions on bare SiO_2 to minimize the substrate swelling/re-deposition as the sputtering of substrate atoms is a major source of indirect damage to graphene[24]. The milling profile was measured using tapping mode atomic force microscope (AFM) which has a tip diameter of ~87 nm. Fig. 2a and b show grey scale AFM topographic images of milled 30 nm–wide and 100 nm-wide trenches in SiO_2, respectively. We found an angle-dependent swelling effect, as can be seen from the AFM cross-section profile shown in the inset of Fig. 2a and b. The swelling is only completely eliminated for tilt angle equal to or larger than 43°. Further tilting broadens the beam spot and thus reduce the resolution. As a result, we use 43° as an optimum tilt. Fig. 2c, shows the swelling height as a function of the applied dose for two different angles: 0° and 43°. Here, positive y values indicate

swelling/deposition while negative values mean etching. At zero tilt (i.e. He^+ ion beam is normal to the sample surface), the swelling height increases with the irradiation dose. Only at very low dose (<1×1018 ions/cm^2) can the substrate be milled. By contrast, when the beam is tilted by 43^o, the substrate can be etched without swelling and the etching depth is increasing with the applied dose, as one would expect. We used the same tilt angles to pattern boxes with different side width W up to 500nm at 1.2×1018 ions/cm^2 (Fig. 2d). At zero tilt, the swelling height scales linearly with W. On the other hand, for 43^o tilted beam, although the etching depth slightly decreases with W, swelling was not observed (Fig. 2c, d). As a result, we chose a beam angle of 43^o and irradiation dose of 6.24×1017 ions/cm^2 (1 nC/um^2) to directly carve graphene.

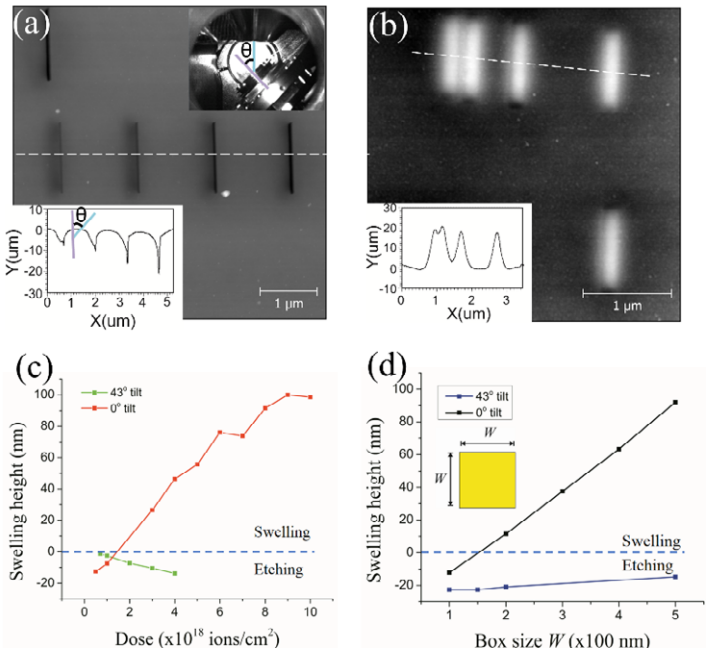

Fig. 2. (a) AFM image of HIM-patterned 30nm lines of SiO_2 at 43^o tilt with dose varying from 0.4×10^{18} to 2.5×10^{18} ions/cm^2. Lower inset shows the cross section profile along the dashed line in the main figure. Upper inset in (a) is the chamber view of a HIM showing a stage tilted by an angle . The blue lines show the orientation of the incident beam. (b) AFM image of HIM-patterned 100nm lines of SiO_2 at 0^o tilt, 1.2×10^{18} ions/cm^2 with various separaton distances. Inset

shows the cross section profile along the dashed line in the main figure. (c-d) Swelling height plots as a function of (c) irradiation dose and (d) box size (*W*) for 0^{o} and 43^{o} tilt beam.

As a result, we chose a beam angle of 43^{o} and irradiation dose of 6.24×10^{17} ions/cm^2 (1 nC/um^2) to directly carve graphene. The milling profile was also measured using tapping mode atomic force microscope (AFM). Raman spectrum was acquired using a confocal Raman microscope (RENISHAW inVia^{TM}) with a ×100 lens (numerical aperture 0.8) and a 532 nm (2.33eV) laser, giving a finite spot radius of ~400 nm. Raman map was obtained over a range spanning from 1000 cm^{-1} to 2100 cm^{-1}, covering the D peak, G peak and D' peak. The distance between each data point is 100 nm. The laser power is maintained at 2mW to prevent thermal heating on the sample surface.

3. Results and discussion

Fig. 3a shows the AFM image of a monolayer graphene with a 35 nm wide line carved by HIM. The measured graphene thickness is ~1nm, slightly thicker than clean graphene. This is mainly due to the moisture covering the surface since our measurement was conducted in ambient environment. We adjusted the beam focus at the edges of the graphene prior to milling in the bulk area therefore the corners are flatter owing to a beam-induced cleaning. The inset shows the cross section view of the milled line in Fig. 3a that presents an asymmetric 'V' shaped feature where the slope is less sharp on the LHS of the carved line (a dip at the center). We attribute this to the structural change in the substrate at the LHS, as will be discussed at the end of this section.

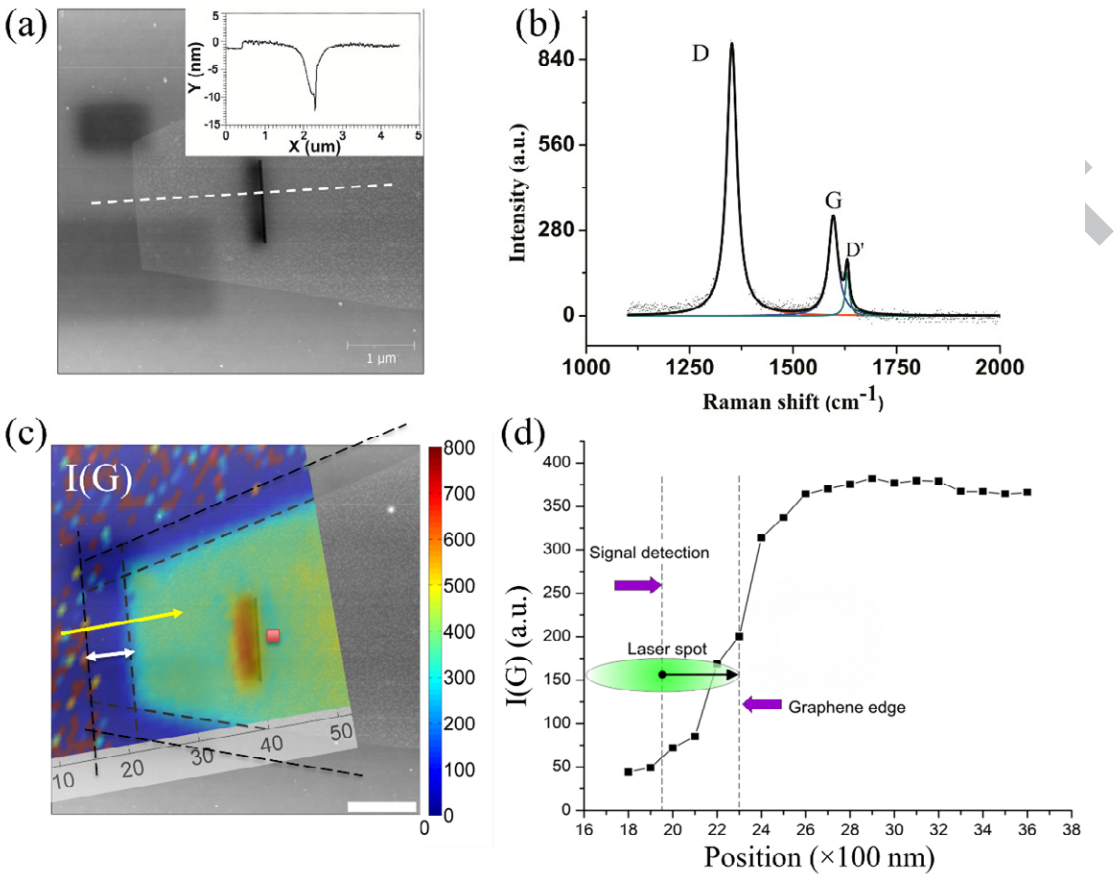

Fig. 3. (a) AFM image of the graphene with a 30 nm line carved by HIM at 43°, 6.24×10^{17} ions/cm^2 dose. The dark squares at the two corners indicate lower topology due to beam-induced cleaning and etching. Inset: the cross section profile along the white dashed line. (b) The Raman spectra of a point near the milling site (the red dot in (c)) is fitted with three Lorentzian curves centered at corresponding peak positions. (c) Raman mapping on top of AFM image of the same area shown in (a). Outer and inner black dashed lines labelled the onset of I(G) and actual edge of the flake, respectively. White double-arrow indicates the inter-line distance of ~400 nm. (d) I(G) values along the yellow arrow across the graphene edge shown in (c).

Raman spectrum at each data point was fitted with three Lorentzians centered at corresponding peak positions as shown in Fig. 3b. We used the I(G) map, shown in Fig. 3c, to determine the boundaries of graphene because I(G) does not depend on edge type unlike I(D)

[40]. In Fig. 3 d we plot the I(G) values across the edge along the yellow arrow shown in Fig. 3c. The edge is defined as the position where I(G) is roughly half of its value inside the flake [40]. This position is ~400nm from where I(G) starts to increase, consistent with the spot size of our laser. Lastly the Raman map is scaled and aligned with the AFM graph to form a hybrid Raman-topographical image.

Two observations can be made from Fig. 3c. Firstly, I(G) is almost constant across the whole flake except an area of 300nm wide at the left of the carved line. I(G) should not change too much at Stage 1 disorder. However at Stage 2, I(G) is expected to increase due to 1) merging of G and D' bands, as can be seen from Fig. 3b and 2) broadening of D band. Secondly, the high I(G) region (orange color in Fig. 3c) does not center at the carved line but it is located along the left edge. This is not due to the error caused by manual aligning since the method we described above is fairly accurate. Interestingly, the AFM data shows lower topology at the same location. Therefore we attribute this asymmetric feature to our milling technique where a tilt beam is applied.

We also observe that (G) always increases with disorder[34,35,45,46]. Therefore we use (G) map to partition the flake into five regions (A-E) for the convenience of analysis (Fig. 4). Region A spans 300nm to the left of the carved line. Region B covers the carved line and a 250nm wide region to the right of it Region C and D are where the beam focus is adjusted at high resolution (irradiation dose ~ 8×10^{15} ions/cm^2). E is far from the carved line where less irradiation was introduced. As can be seen from the colored map, graphene in region A has the largest disorder as $(G)_A$ ~ 60 cm^{-1}. The graphene near the milling, i.e., region B shows overall less disorder: $(G)_B$ ~ 40 cm^{-1}. It is usually a good practice to focus the beam near the target site to achieve the best resolution for the actual milling. Focusing on the graphene creates moderate

damage at C and D: $(G)_C$ ~ 33 cm^{-1} and $(G)_D$ ~ 50 cm^{-1} . Graphene lattice is much preserved in E as $(G)_E$ is only around 13 cm^{-1}.

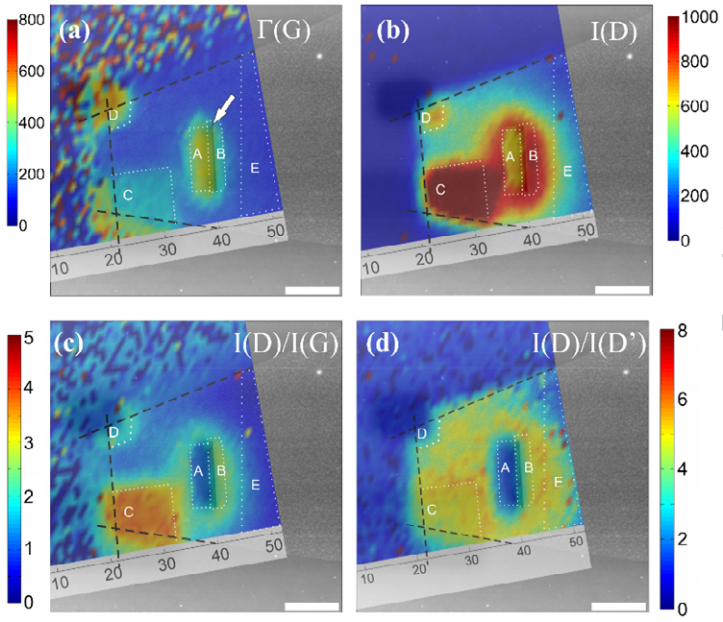

Fig. 4. (a-d) Mappings of (G), I(D), I(D)/I(G) and I(D)/I(D') on top of the AFM image shown in figure 3a. The unit of the Raman mapping axis is 100nm. Scale bar is 1μm. White dashed lines define the following five regions of interest: A is a 300nm wide area at the LHS adjacent to the carved line. B is an 250nm wide region at RHS containing the carved line (pointed by the white arrow in (a)). C and D are regions where beam focusing was adjusted.

Fig. 4b shows the map of I(D) whose evolution tracks the development of disorder in the graphene lattice. D should increase with the defect density in Stage 1 and starts decreasing in Stage 2 due to the loss the hexagonal rings, according to the local activation model [34,35]. In order to derive the L_D in the defective regions induced by He^+ ion bombardment, the spatial map of I(D)/I(G) is obtained as shown in Fig. 4c. Unlike the monotonic increase of (G) towards region A, I(D)/I(G) near region A has a 'ring' shape. At the center of the ring (i.e., region A), I(D)/I(G) reaches the lowest $I(D)/I(G)_A$ ~ 1. At the body of the ring (i.e., region B), $I(D)/I(G)_B$ reads ~2.5. I(D)/I(G) has a peak value at region C, $I(D)/I(G)_C$ ~ 4. Combining this with the (G)

data, we can conclude that region B is in Stage 1 disorder while A and D are in Stage 2 disorder. C is near the transition between Stage 1 and Stage 2 disorder. This is done by finding the corresponding L_D of each I(D)/I(G) using equation 1.

Fig. 5 shows the plot of equation 1, with r_S=1nm and r_A=3nm. C_A depends on excitation energy and is experimentally fit by $C_A = 160E_L^{-4}$ where E_L=2.33eV being the laser energy[35]. C_S has a value of 0.87 and 0, as was determined experimentally in reference[34] and reference[35], respectively. In Stage 1, C_S should account for less than 10% variation of I(D)/I(G), therefore it is safe to set $C_S = 0$ for all defect types[38]. However in stage 2, C_S has a more significant influence on I(D)/I(G) since it dictates the minimum value of I(D)/I(G) in this stage when $L_D \rightarrow 0$. In our case, I(D)/I(G)>1 is always observed in the most defective region, i.e., region A where I(D)/I(G) bounced back from the maxima implying that C_S has a finite value of ~1 . As displayed in Fig. 5, L_D in different regions can be estimated: $L_{D(A)}$~1.5 nm, $L_{D(B)}$~8.5 nm, $L_{D(C)}$ is either ~4.0 nm or ~7.0 nm, $L_{D(D)}$~2.5 nm. Note it is not possible to unambiguously discriminate between the two disorder stages for region C due to the lack of data near the transition point.

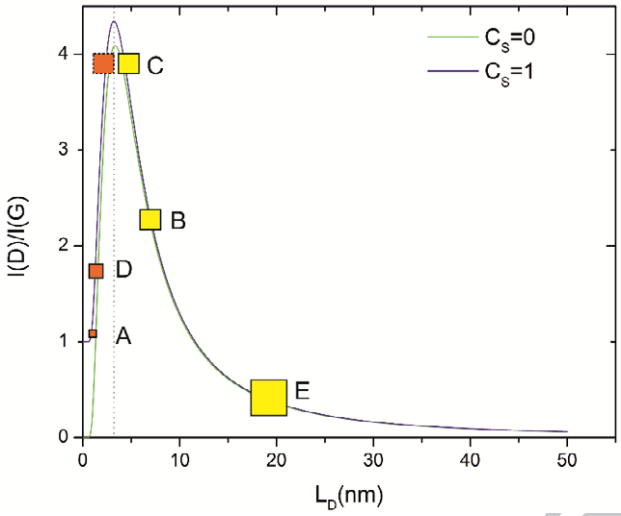

Fig. 5. Plot of equation 1 with Cs = 0 (green curve) and Cs = 1 (violet curve). Stage 1 disordered regions are illustrated as yellow boxes while Stage 2 disorderd regions are shown as orange boxes. The size of the boxes indicate the deviation of data in these regions.

It is surprising that although the designed pattern is 35 nm wide, the defective region after milling extends to 300nm to the left (region A) and 250nm to the right (region B). However, the exact length scale cannot be determined owing to the resolution (~400nm) of our Raman spectroscopy. Techniques such as tip enhanced Raman spectroscopy (TERS) can be employed where a much higher lateral resolution is provided by an AFM [47,48].

Reference [38,39] demonstrated that D' depends on the disorder structure and thus I(D)/I(D') can be used to experimentally determine the defect type in graphene. Fig. 4d shows the I(D)/I(D') map of the same sample. The value of I(D)/I(D') is ~ 7 for vacancy-type defect created by Ar^+ bombardment, 3.5 for boundary-like defects in graphite and 13 for sp^3-type defect, as observed in reference [39]. In the map shown in Fig. 4d we see that the area surrounding the milled graphene has value of about 5 of the ratio I(D)/I(D'). We also notice that this ratio is very small for region A with high defect density and for region B. Therefore, we deduce that in our case the graphene lattice near the milling site can consist of multiple types of defects, i.e. a

mixture of vacancies (single, double and complex) and amorphised area[49]. However, it is not possible to attain information on defect type from I(D)/I(D') values for Stage 2 disorder regions (A and D) because defect structure is no longer complete at extremely high defect density[39].

To understand why He^+ milling caused such distribution of damage in graphene and more specifically, to find out the interaction between the He^+ beam and the substrate, a Monte Carlo simulation on the stopping range of ions using SRIM package [50] was conducted. The simulator tracks the trajectories of 10^5 He^+ ions with 30keV energy incident 43^o to the target. The target consists of a 0.35nm thick carbon layer, 300nm SiO_2 and 700nm Si. In order to mimic the graphene supported by SiO_2, modifications have been made to the graphite layer. Since graphene binds weakly to the SiO_2, we changed the surface binding energy E_B to 15meV from previous first principle calculations[51]. We also changed the displacement threshold energy T_d to 68eV as more energy is required to displace C atom in supported graphene compared to suspended graphene [24]. Here we consider a stable configuration where an O atom on the SiO_2 surface (either O-terminated or OH-terminated) is below the hollow site of C hexagonal ring [24,51]. As shown in Fig. 6a, most He^+ ions stop at around 250nm inside the oxide. Although only 3% of incident He^+ ions were backscattered to the surface, almost all of these ions escaped the surface from the LHS of the milled line within 100-300 nm of the ion incident location, consistent with the size of region A. This could be a potential source of defect formation in region A as these escaped He^+ ions remain energetic with a large scattering cross-section. In addition to backscattered ions, recoiled Si and O atoms that reach the surface should also be responsible for the indirect damage in graphene lattice [24]. Our simulation shows the sputtering yield for Si and O are 0.026 and 0.034, respectively. Most of these recoil atoms have energy larger than 3eV, being able to generate various types of defects[52]. The simulation is repeated with a normal angle of incident as shown in Fig. 6b. The insets show the ion distribution at the surface.

Although the angled case show large ion density at the LHS, the number of ions that stopped at RHS is significantly reduced in comparison to the non-tilt case.

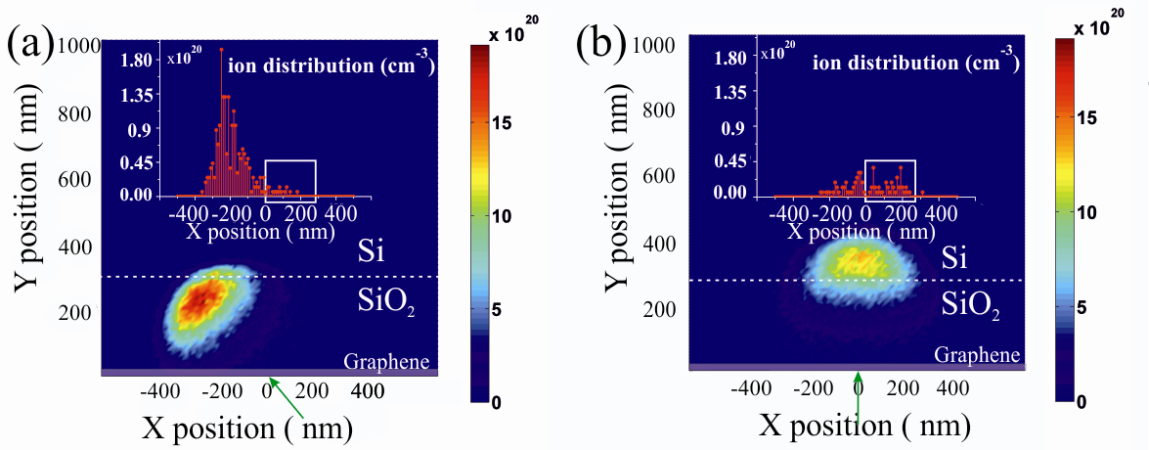

Fig. 6. SRIM simulation of He^+ ions distribution inside the Graphene-SiO_2(300nm)-Si(700nm) volume with a dose equal to 6.27×10^{17} ions/cm^{-3} for two different incident angles: (a) 43° tilt (b) 0° tilt. The white dashed lines indicate the interface between Si and SiO_2. Green arrows point at the incident point following the beam direction. The insets show the backscattered ion distribution at the surface. The white rectangles outlines the distance 280nm to the right of incident point showing distinct difference in the backscattered ion distribution.

We repeated the above-mentioned angled milling technique on graphene with doses close to but smaller the threshold value we found for complete carving (~6.24×10^{17} ions/cm^2). The line width is 5 nm. As can be seen from the AFM image (Fig. 7a), the tearing of graphene sheet has not developed thoroughly but the adjacent area has already shown wide structural change. (G) and I(D)/I(G) measured at the LHS of the groove are plotted in Fig. 7b as functions of the irradiation dose. The increase of FWHM with the dose is attributed to the indirect damage by the sputtering of underlying SiO_2 and backscattered He^+ ions. The I(D)/I(G) data shows a peak value of ~1.9 at 3.74×10^{17} ions/cm^2 where (G) is around 29. This is in reasonable agreement with the maximum I(D)/I(G) of 4 where (G) is 33 as found in Region C shown in Fig. 4, implying the

indirect damage caused by such dose level is comparable to the damage caused by direct exposure of He^+ ions at ~8×10^{15} ions/cm^2.

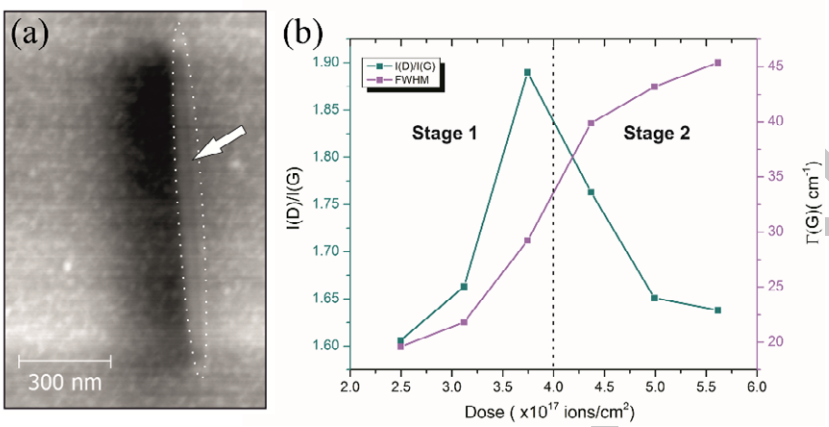

Fig. 7. (a) AFM image of this sample where a 5nm groove (enclosed by the white dashed ellipse) starts to appear after irradiation of He^+ ions at 4.4×10^{17} ions/cm^2. (b) I(D)/I(G) (cyan) and (G) (purple) measured for another sample milled with a set of doses lower than the threshold value.

It has been found that the as-fabricated down-scaled graphene nano-electronic devices no longer shows characteristics of graphene such as gate tunability, after being carved by a well-focused He^+ ion beam[42]. This is shown in Fig. 8a where a U-shape GNR channel was fabricated by He^+ milling. The IV characteristic is linear showing a resistance of ~1M , but no gate modulation was observed (at negligible gate leakage). We attribute this to the highly disordered carbon network caused by milling at 0^o angle of incident. We hereby propose a novel fabrication technique that dynamically tilts the beam in order to shift the damage of the backscattered ions and sputtered atoms to the far side of the active region, thus preserving the channel itself. This is schematically illustrated in Fig. 8b. Also shown Monte Carlo simulation of incident ions trajectories. For instance, the beam will be tilted twice to mill at both sides of a GNR. As can be seen from Fig. 8c, our method effectively avoid the damage in the center

channel region while milling from a normal direction has equal damage on both sides of the beam.

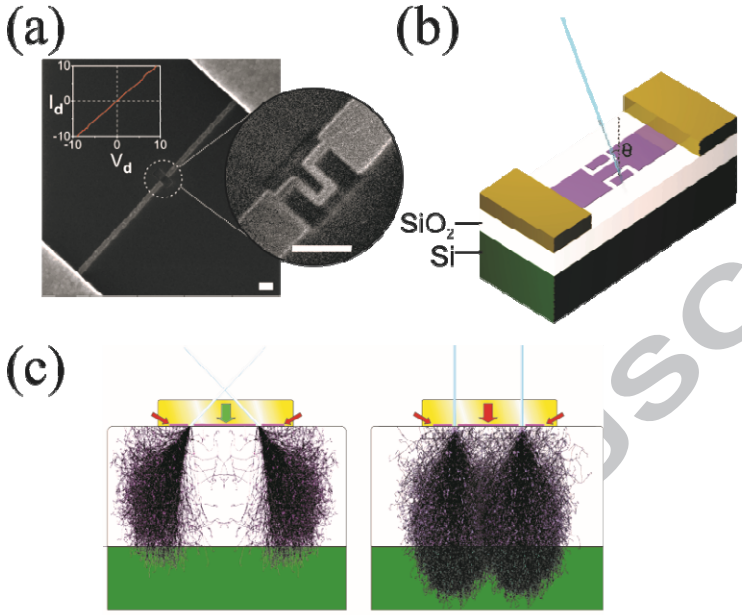

Fig. 8. (a) The HIM image of a 50nm wide U-shape channel carved on a GNR. Both scale bars are 200nm. The inset is the drain-source IV curve. (b) Schematic of a GNR device being carved by a tilt He^+ ion beam. (c) Schematic drawing of the He^+ carving of a graphene device using a tilted and a non-tilted beam. Also shown the He^+ ions trajectories inside the substrate, calculated using Monte Carlo simulation. Green and red arrows point at the preserved graphene and highly damaged graphene, respectively.

4. Conclusions

We performed a 30 keV He^+ beam tilt-dependent controlled milling of graphene on SiO_2. We found an optimum beam tilt angle of 43°, whereby the swelling of the substrate was effectively eliminated and the damage to non-milled areas of graphene minimized. Spatially resolved Raman spectrum near the milling site indicates an asymmetric defect distribution where Stage 2 disorder (L_D~1.5nm) was found along the direction of incident beam and Stage 1 disorder (L_D~8.5nm) on the other side. The defective region spans ~ 300nm and ~ 250 nm on

each side of the milling site. We attributed the formation of these damaged regions to 1) backscattered He^+ ions and 2) recoil substrate atoms. Our work provides knowledge for the characterization of damage induced in ion-beam associated patterning of graphene, which is essential for the downscaling of electronic, spintronic and quantum devices on any 2-D materials.

5. Acknowledgement

The authors would like to acknowledge useful discussion with H. Chong, S. Saito, Y. Tsuchiya and help from Dr. S. Boden, P. Ayliffe on fabrication process and partial financial support from Hitachi Cambridge lab and the Grants-in-Aid for Scientific Research from the Ministry of Education, Culture, Sports, Science and Technology (MEXT) in Japan (KAKENHI No. 25220904).

6. Reference

[1] Novoselov KS, Geim AK, Morozov SV, Jiang D, Katsnelson MI, Grigorieva IV, et al. Two-dimensional gas of massless Dirac fermions in graphene. Nature 2005;438:197–200.

[2] Morozov S, Novoselov K, Katsnelson M, Schedin F, Elias D, Jaszczak J, et al. Giant Intrinsic Carrier Mobilities in Graphene and Its Bilayer. Phys Rev Lett 2008;100:016602.

[3] Geim AK, Novoselov KS. The rise of graphene. Nat Mater 2007;6:183–91.

[4] Bonaccorso F, Sun Z, Hasan T, Ferrari AC. Graphene photonics and optoelectronics. Nat Photonics 2010;4:611–22.

[5] Lee C, Wei X, Kysar JW, Hone J. Measurement of the elastic properties and intrinsic strength of monolayer graphene. Science 2008;321:385–8.

[6] Novoselov KS, Geim AK, Morozov SV, Jiang D, Zhang Y, Dubonos SV, et al. Electric field effect in atomically thin carbon films. Science 2004;306:666–9.

[7] Han MY, Özyilmaz B, Zhang Y, Kim P. Energy Band-Gap Engineering of Graphene Nanoribbons. Phys Rev Lett 2007;98:206805.

[8] Trauzettel B, Bulaev DV., Loss D, Burkard G. Spin qubits in graphene quantum dots. Nat Phys 2007;3:192–6.

[9] Molitor F, Knowles H, Dröscher S, Gasser U, Choi T, Roulleau P, et al. Observation of excited states in a graphene double quantum dot. Eur Lett 2010;89:67005.

[10] Ponomarenko LA, Schedin F, Katsnelson MI, Yang R, Hill EW, Novoselov KS, et al. Chaotic Dirac billiard in graphene quantum dots. Science 2008;320:356–8.

[11] Connolly MR, Chiu KL, Giblin SP, Kataoka M, Fletcher JD, Chua C, et al. Gigahertz quantized charge pumping in graphene quantum dots. Nat Nanotechnol 2013;8:417–20.

[12] Cai J, Ruffieux P, Jaafar R, Bieri M, Braun T, Blankenburg S, et al. Atomically precise bottom-up fabrication of graphene nanoribbons. Nature 2010;466:470–3.

[13] Blankenburg S, Cai J, Ruffieux P, Jaafar R, Passerone D, Feng X, et al. Intraribbon heterojunction formation in ultranarrow graphene nanoribbons. ACS Nano 2012;6:2020–5.

[14] Picakrd D, Scipioni L. Graphene Nano-Ribbon Patterning in the ORION ® PLUS. Zeiss Appl Note 2009.

[15] Fischbein MD, Drndić M. Electron beam nanosculpting of suspended graphene sheets. Appl Phys Lett 2008;93:113107.

[16] Lemme MC, Bell DC, Williams JR, Stern LA, Baugher BWH, Jarillo-Herrero P, et al. Etching of graphene devices with a helium ion beam. ACS Nano 2009;3:2674–6.

[17] Boden SA, Moktadir Z, Bagnall DM, Mizuta H, Rutt HN. Focused helium ion beam milling and deposition. Microelectron Eng 2011;88:2452–5.

[18] Bell DC, Lemme MC, Stern LA, Williams JR, Marcus CM. Precision cutting and patterning of graphene with helium ions. Nanotechnology 2009;20:455301.

[19] Volk C, Fringes S, Terrés B, Dauber J, Engels S, Trellenkamp S, et al. Electronic excited states in bilayer graphene double quantum dots. Nano Lett 2011;11:3581–6.

[20] Dean CR, Young AF, Meric I, Lee C, Wang L, Sorgenfrei S, et al. Boron nitride substrates for high-quality graphene electronics. Nat Nanotechnol 2010;5:722–6.

[21] Bresnehan MS, Hollander MJ, Wetherington M, Labella M, Trumbull KA, Cavalero R, et al. Integration of Hexagonal Boron Nitride with Quasi-freestanding Epitaxial Graphene: Toward Wafer-Scale, High-Performance Devices. ACS Nano 2012;6:5234–41.

[22] Goossens ASM, Driessen SCM, Baart TA, Watanabe K, Taniguchi T, Vandersypen LMK. Gate-defined confinement in bilayer graphene-hexagonal boron nitride hybrid devices. Nano Lett 2012;12:4656–60.

[23] Tseng AA. Recent developments in nanofabrication using focused ion beams. Small 2005;1:924–39.

[24] Zhao S, Xue J, Wang Y, Yan S. Effect of SiO_2 substrate on the irradiation-assisted manipulation of supported graphene: a molecular dynamics study. Nanotechnology 2012;23:285703.

[25] Meyer JC, Kisielowski C, Erni R, Rossell MD, Crommie MF, Zettl a. Direct imaging of lattice atoms and topological defects in graphene membranes. Nano Lett 2008;8:3582–6.

[26] Meyer JC, Eder F, Kurasch S, Skakalova V, Kotakoski J, Park HJ, et al. Accurate Measurement of Electron Beam Induced Displacement Cross Sections for Single-Layer Graphene. Phys Rev Lett 2012;108:196102.

[27] Tan YW, Stormer HL, Kim P, Novoselov KS, Cohen ML, Louie SG, et al. Graphene at the Edge•: Stability and Dynamics. Science (80-) 2009;666:1705–8.

[28] Kurasch S, Kotakoski J, Lehtinen O, Skákalová V, Smet J, Krill CE, et al. Atom-by-atom observation of grain boundary migration in graphene. Nano Lett 2012;12:3168–73.

[29] Mølhave K, Gudnason SB, Pedersen AT, Clausen CH, Horsewell A, Bøggild P. Electron irradiation-induced destruction of carbon nanotubes in electron microscopes. Ultramicroscopy 2007;108:52–7.

[30] Barreiro A, Börrnert F, Avdoshenko SM, Rellinghaus B, Cuniberti G, Rümmeli MH, et al. Understanding the catalyst-free transformation of amorphous carbon into graphene by current-induced annealing. Sci Rep 2013;3:3–8.

[31] Ferrari AC, Meyer JC, Scardaci V, Casiraghi C, Lazzeri M, Mauri F, et al. Raman Spectrum of Graphene and Graphene Layers. Phys Rev Lett 2006;187401:1–4.

[32] Ferrari AC, Basko DM. Raman spectroscopy as a versatile tool for studying the properties of graphene. Nat Nanotechnol 2013;8:235–46.

[33] Ryu S, Maultzsch J, Han MY, Kim P, Brus LE. Raman Spectroscopy of Lithographically Patterned Graphene Nanoribbons 2011;5:4123–30.

[34] Lucchese MM, Stavale F, Ferreira EHM, Vilani C, Moutinho MVO, Capaz RB, et al. Quantifying ion-induced defects and Raman relaxation length in graphene. Carbon N Y 2010;48:1592–7.

[35] Cançado LG, Jorio A, Ferreira EHM, Stavale F, Achete CA, Capaz RB, et al. Quantifying defects in graphene via Raman spectroscopy at different excitation energies. Nano Lett 2011;11:3190–6.

[36] Tuinstra F. Raman Spectrum of Graphite. J Chem Phys 1970;53:1126.

[37] Das A, Pisana S, Chakraborty B, Piscanec S, Saha SK, Waghmare UV, et al. Monitoring dopants by Raman scattering in an electrochemically top-gated graphene transistor. Nat Nanotechnol 2008;3:210–5.

[38] Eckmann A, Felten A, Verzhbitskiy I, Davey R, Casiraghi C. Raman study on defective graphene: Effect of the excitation energy, type, and amount of defects. Phys Rev B 2013;88:035426.

[39] Eckmann A, Felten A, Mishchenko A, Britnell L, Krupke R, Novoselov KS, et al. Probing the Nature of Defects in Graphene by Raman Spectroscopy. Nano Lett 2012;12:3925–30.

[40] Casiraghi C, Hartschuh A, Qian H, Piscanec S, Georgi C, Fasoli A, et al. Raman Spectroscopy of Graphene Edges. Nano Lett 2009;9:1433–41.

[41] Fox D, Zhou YB, O'Neill A, Kumar S, Wang JJ, Coleman JN, et al. Helium ion microscopy of graphene: beam damage, image quality and edge contrast. Nanotechnology 2013;24:335702.

[42] Kalhor N, Boden SA, Mizuta H. Sub-10 nm patterning by focused He-ion beam milling for fabrication of downscaled graphene nano devices. Microelectron Eng 2014;114:70–7.

[43] Winston D, Cord BM, Ming B, Bell DC, DiNatale WF, Stern LA, et al. Scanning-helium-ion-beam lithography with hydrogen silsesquioxane resist. J Vac Sci Technol B Microelectron Nanom Struct 2009;27:2702.

[44] Nakaharai S, Iijima T, Ogawa S, Suzuki S, Li S, Tsukagoshi K. Conduction Tuning of Graphene Based Defect-induced Localization. ACS Nano 2013;7:5694–700.

[45] Cançado L, Jorio A, Pimenta M. Measuring the absolute Raman cross section of nanographites as a function of laser energy and crystallite size. Phys Rev B 2007;76:064304.

[46] Martins Ferreira EH, Moutinho MVO, Stavale F, Lucchese MM, Capaz RB, Achete CA, et al. Evolution of the Raman spectra from single-, few-, and many-layer graphene with increasing disorder. Phys Rev B 2010;82:125429.

[47] Ghislandi M, Hoffmann GG, Tkalya E, Xue L, With G De. Tip-Enhanced Raman Spectroscopy and Mapping of Graphene Sheets. Appl Spectrosc Rev 2012;47:371–81.

[48] Cançado LG, Hartschuh A, Novotny L. Tip-enhanced Raman spectroscopy of carbon nanotubes. J Raman Spectrosc 2009;40:1420–6.

[49] Lehtinen O, Kotakoski J, Krasheninnikov AV, Keinonen J. Cutting and controlled modification of graphene with ion beams. Nanotechnology 2011;22:175306.

[50] Ziegler JF, Ziegler MD, Biersack JP. SRIM – The stopping and range of ions in matter (2010). Nucl Instruments Methods Phys Res Sect B Beam Interact with Mater Atoms 2010;268:1818–23.

[51] Nguyen TC, Otani M, Okada S. Semiconducting Electronic Property of Graphene Adsorbed on (0001) Surfaces of SiO_2. Phys Rev Lett 2011;106:106801.

[52] Banhart F, Kotakoski J, Krasheninnikov AV. Structural defects in graphene. ACS Nano 2011;5:26–41.